



**HAL**  
open science

## Long-lifetime coherence in a quantum emitter induced by a metasurface

Emmanuel Lassalle, Philippe Lalanne, Syed Aljunid, Patrice Genevet, Brian Stout, Thomas Durt, David Wilkowski

► **To cite this version:**

Emmanuel Lassalle, Philippe Lalanne, Syed Aljunid, Patrice Genevet, Brian Stout, et al.. Long-lifetime coherence in a quantum emitter induced by a metasurface. *Physical Review A*, 2020, 101 (1), 10.1103/PhysRevA.101.013837 . hal-02997834

**HAL Id: hal-02997834**

**<https://hal-iogs.archives-ouvertes.fr/hal-02997834v1>**

Submitted on 10 May 2021

**HAL** is a multi-disciplinary open access archive for the deposit and dissemination of scientific research documents, whether they are published or not. The documents may come from teaching and research institutions in France or abroad, or from public or private research centers.

L'archive ouverte pluridisciplinaire **HAL**, est destinée au dépôt et à la diffusion de documents scientifiques de niveau recherche, publiés ou non, émanant des établissements d'enseignement et de recherche français ou étrangers, des laboratoires publics ou privés.

**Long-lifetime coherence in a quantum emitter induced by a metasurface**Emmanuel Lassalle <sup>1,\*</sup>, Philippe Lalanne,<sup>2</sup> Syed Aljunid <sup>3</sup>, Patrice Genevet,<sup>4</sup> Brian Stout,<sup>1</sup> Thomas Durt,<sup>1</sup> and David Wilkowski<sup>3,5,6,†</sup><sup>1</sup>*Aix Marseille Univ, CNRS, Centrale Marseille, Institut Fresnel, F-13013 Marseille, France*<sup>2</sup>*LP2N, Institut d'Optique Graduate School, CNRS, Université Bordeaux, F-33400 Talence, France*<sup>3</sup>*Centre for Disruptive Photonic Technologies, TPI and SPMS Nanyang Technological University, 637371 Singapore*<sup>4</sup>*CRHEA, CNRS, Université Côte-d'azur, 06560 Valbonne, France*<sup>5</sup>*Centre for Quantum Technologies, National University of Singapore, 117543 Singapore*<sup>6</sup>*MajuLab, International Joint Research Unit UMI 3654, CNRS, Université Côte d'Azur, Sorbonne Université, National University of Singapore, Nanyang Technological University, Singapore*

(Received 5 September 2019; revised manuscript received 16 December 2019; published 31 January 2020)

An anisotropic quantum vacuum (AQV) has been predicted to induce quantum interferences during the spontaneous emission process in an atomic  $V$  transition [G. S. Agarwal, *Phys. Rev. Lett.* **84**, 5500 (2000)]. Nevertheless, the finite lifetime of the excited states is expected to strongly limit the observability of this phenomenon. In this paper, we predict that an AQV can induce a long-lifetime coherence in an atomic  $\Lambda$  transition from the process of spontaneous emission, which has an additional advantage of removing the need for coherent laser excitation. We also carry out two metasurface designs and compare their respective efficiencies for creating an AQV over remote distances. The detection of this coherence induced by a metasurface, in addition to being yet another vindication of quantum electrodynamics, could pave the way towards the remote distance control of coherent coupling between quantum emitters, which is a key requirement to produce entanglement in quantum technology applications.

DOI: [10.1103/PhysRevA.101.013837](https://doi.org/10.1103/PhysRevA.101.013837)**I. INTRODUCTION**

The control of the spontaneous emission of quantum emitters (QEs) has been investigated principally in a confined volume by the cavity-quantum electrodynamics community [1], the archetype of which is a cavity formed by perfect mirrors. The notion of “cavity” was then generalized to open resonators by the nanophotonics community [2], where strong couplings can be achieved. However, this typically only occurs in the near field of the photonic nanostructure and vanishes beyond a distance  $d \sim \lambda_0$ , where  $\lambda_0$  is the emission wavelength of the QE in vacuum.

There are a few other optical systems that can affect the spontaneous emission of QEs in the far field ( $d \gg \lambda_0$ ). For instance, when covering half of the QE emission solid angle with a *spherical mirror*, it has been predicted that the vacuum fluctuations can be fully suppressed at remote distances within a volume  $\approx \lambda_0^3$ , leading to a total inhibition of the decay of a two-level atom [3]. In a classical picture, the field reflected by the spherical mirror can fully interfere with the direct field emitted by the atom: If the atom is located at the focus of the spherical mirror such that  $d = n\lambda_0/2$  with  $n$  an integer number, there is a complete suppression of the spontaneous emission, whereas if the atom is at the position  $d = (n + 1/2)\lambda_0/2$  the spontaneous emission is enhanced by a factor of 2. Such effects occur provided that the round trip time of

flight for the light to go from the atom to the mirror and back is shorter than the atom decay time  $1/\gamma_0$  (with  $\gamma_0$  the decay rate in free space), that is, for distances  $d$  smaller than the *photonic coherence length*  $d_{CL} \equiv c/2\gamma_0$  [4,5]. Such an alteration of the decay rate was already reported in [6], where the authors measured 1% change in the decay rate of an ion located at 30 cm from a mirror.

More recently, it has been suggested to use a reflecting metasurface acting as a spherical mirror to modify the spontaneous emission of a multilevel QE located at remote distances [7,8]. This new paradigm unites the quantum optics and metasurface communities [9,10], and relies on the fact that reflecting metasurfaces made of nanoresonators can break the isotropic nature of the vacuum to induce a polarization-dependent response, thus creating an anisotropic quantum vacuum (AQV). It was previously predicted that an AQV can lead to quantum interferences in orthogonal levels of a multilevel QE in a  $V$  configuration, that is, two excited states and one ground state [11]. However, the predicted effects, i.e., a population transfer between the two excited states of  $\approx 1\%$  [7] and an induced coherence of about 10% [8], only last as long as the atom remains in its excited states, which is a drastic drawback for experimental confirmations.

Although the  $V$  scheme is the one most often considered in the literature [7,8,11–16], this paper focuses on the spontaneous emission properties of a QE with a  $\Lambda$  transition, i.e., a single excited state linked to two nearly degenerate ground states, in an AQV created by a metasurface. We predict the generation of a coherence between the two ground states, which survives after the photon emission. The interest

\*emmanuel.lassalle@fresnel.fr

†david.wilkowski@ntu.edu.sg

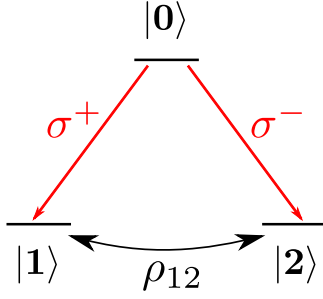


FIG. 1. Three-level quantum emitter with a  $\Lambda$  structure. The upper level  $|0\rangle$  can decay via two transitions: either to the state  $|1\rangle$  with the emission of a right circularly polarized photon denoted  $\sigma^+$ , or to the state  $|2\rangle$  with the emission of a left circularly polarized photon denoted  $\sigma^-$ .  $\rho_{12}$  denotes the coherence between the two ground states  $|1\rangle$  and  $|2\rangle$ .

in the ground-state coherence arises from its long lifetime, which allows high-resolution experiments. Moreover, it was previously known that this coherence could only be generated with an external coherent laser field (see [17], Chap. 3). Here, we show that such a coherence can be simply generated by spontaneous emission in an anisotropic vacuum (in the absence of a laser field).

In Sec. II, we derive the master equation for the  $\Lambda$  scheme (Sec. II A), and we show how an anisotropic vacuum can induce a coherence between the ground states from the process of spontaneous emission (Sec. II B). We also provide an interpretation of this result in terms of the dressed states of the system (Sec. II C). In Sec. III, following a phase-mapping approach (presented in Sec. III A), we propose two designs of metasurfaces to realize the anisotropic vacuum and characterize their performances (Secs. III B and III C). Finally, we assess the value of the coherence that can be achieved using such metasurfaces, taking into account the limitations due to the finite size of their nanoresonators (Sec. IV).

## II. THEORETICAL PREDICTION: LONG-LIFETIME COHERENCE

We consider a three-level system in a so-called  $\Lambda$  scheme: one single excited state  $|0\rangle$ , which can decay into two ground states  $|1\rangle$  and  $|2\rangle$  via two orthogonal dipolar transitions by the emission of circularly polarized photons  $\sigma^+$  and  $\sigma^-$ , respectively (see Fig. 1). By orthogonal transitions, we mean that the dipole moments  $\mathbf{d}_{01}$  and  $\mathbf{d}_{02}$  corresponding to these transitions are orthogonal (i.e.,  $\mathbf{d}_{01}^* \cdot \mathbf{d}_{02} = 0$ ). They are given by  $\mathbf{d}_{01} = +d_{01}\bar{\mathbf{e}}_+$  and  $\mathbf{d}_{02} = -d_{02}\bar{\mathbf{e}}_-$  where  $\bar{\mathbf{e}}_{\pm} = (\bar{\mathbf{x}} \pm i\bar{\mathbf{y}})/\sqrt{2}$ . We use the  $\bar{\mathbf{z}}$  direction as the quantization axis. This scheme appears naturally in nitrogen-vacancy (NV) centers in diamond, using the magnetic sublevels  $|\pm 1\rangle$  as the ground states and  $|A_2\rangle$  as the excited state [18]. It also can be found in atoms, using the Zeeman manifold with  $|F, m = \pm 1\rangle$  for the ground states and  $|F', m = 0\rangle$  for the excited state, where  $m$  denotes the magnetic quantum numbers, and  $F$  and  $F'$  are the total angular momentum quantum numbers [17].

The interaction between the atom (at position  $\mathbf{r}_0$ ) and the electromagnetic (em) environment in the vacuum state (i.e., no photons) is described by the interaction Hamiltonian in the

electric dipole approximation:  $\hat{H}_I = -\hat{\mathbf{d}} \cdot \hat{\mathbf{E}}_v(\mathbf{r}_0)$ . The dipole moment operator  $\hat{\mathbf{d}}$  is given by  $\hat{\mathbf{d}} = \mathbf{d}_{01} |0\rangle \langle 1| + \mathbf{d}_{02} |0\rangle \langle 2| + \mathbf{d}_{01}^* |1\rangle \langle 0| + \mathbf{d}_{02}^* |2\rangle \langle 0|$ . The electromagnetic-field operator  $\hat{\mathbf{E}}_v$  (where the subscript  $v$  denotes the vacuum) can formally be written as a sum of a complex field  $\hat{\mathbf{E}}_v^{(+)}$  and its Hermitian conjugate (H.c.)  $\hat{\mathbf{E}}_v^{(-)} = [\hat{\mathbf{E}}_v^{(+)}]^\dagger$ :  $\hat{\mathbf{E}}_v(\mathbf{r}_0) = \hat{\mathbf{E}}_v^{(+)}(\mathbf{r}_0) + \hat{\mathbf{E}}_v^{(-)}(\mathbf{r}_0)$ . In the interaction picture (time-dependent Hamiltonian), and after making the *rotating wave approximation*, this interaction Hamiltonian reads

$$\begin{aligned} \hat{H}_I(t) = & -(\mathbf{d}_{01} |0\rangle \langle 1| e^{i\omega_1 t} + \mathbf{d}_{02} |0\rangle \langle 2| e^{i\omega_2 t}) \cdot \hat{\mathbf{E}}_v^{(+)}(\mathbf{r}_0, t) \\ & -(\mathbf{d}_{01}^* |1\rangle \langle 0| e^{-i\omega_1 t} + \mathbf{d}_{02}^* |2\rangle \langle 0| e^{-i\omega_2 t}) \cdot \hat{\mathbf{E}}_v^{(-)}(\mathbf{r}_0, t), \end{aligned} \quad (1)$$

where  $\omega_i$  is the transition frequency associated with the transition  $|0\rangle \rightarrow |i\rangle$  ( $i = 1, 2$ ). We derive in Sec. II A the master equation for the reduced density matrix of the atom.

### A. Master equation for the atomic density matrix

The total system (atom plus em environment) is characterized by the density matrix  $\rho_T(t)$ , which obeys the Schrödinger equation, which, in the interaction picture, reads [19,20]

$$\frac{\partial \rho_T(t)}{\partial t} = \frac{1}{i\hbar} [\hat{H}_I(t), \rho_T(t)], \quad (2)$$

with  $\hat{H}_I(t)$  given by Eq. (1). The reduced density matrix of the atom (atomic density matrix) is obtained by taking the trace over the degrees of freedom of the environment:  $\rho(t) \equiv \text{Tr}_e[\rho_T(t)]$ . In order to find the master equation governing the evolution of this reduced density matrix, we first assume that there is no correlation between the atom and the em environment at time  $t = 0$ , so that  $\rho_T(0)$  factorizes as  $\rho_T(0) = \rho(0) \otimes \rho_e(0)$ , with  $\rho_e$  the reduced density matrix of the em environment. Moreover, considering that only the state of the atom is affected by the interaction, we assume that, at later times  $t$ ,  $\rho_T(t)$  factorizes as  $\rho_T(t) = \rho(t) \otimes \rho_e(0)$ . Finally, by making two other major approximations, known as the *Born and Markov approximations*, we obtain the following master equation for the atomic density matrix  $\rho(t)$  (where we have considered for simplicity close-lying states,  $\omega_1 \simeq \omega_2 \equiv \omega_0$ ; see the Appendix for the details of the derivation):

$$\begin{aligned} \frac{\partial \rho(t)}{\partial t} = & -\left[ i\omega_0 + \frac{\gamma_1}{2} + \frac{\gamma_2}{2} \right] |0\rangle \langle 0| \rho(t) \\ & + \rho_{00}(t) \left[ \frac{\gamma_1}{2} |1\rangle \langle 1| + \frac{\gamma_2}{2} |2\rangle \langle 2| \right. \\ & \left. + \frac{\kappa_{21}}{2} |2\rangle \langle 1| + \frac{\kappa_{12}}{2} |1\rangle \langle 2| \right] + \text{H.c.} \end{aligned} \quad (3)$$

In Eq. (3),  $\rho_{00}(t)$  denotes the population in the excited state  $|0\rangle$  (defined as  $\rho_{00}(t) \equiv \langle 0| \rho(t) |0\rangle$ ), and we have introduced the coefficients  $\gamma_i$  and  $\kappa_{ij}$ , the expressions of which are

$$\gamma_i \equiv \frac{1}{\hbar^2} \mathbf{d}_{0i}^* \cdot \hat{\mathbf{C}}(\mathbf{r}_0, \mathbf{r}_0, \omega_0) \cdot \mathbf{d}_{0i} \quad (i = 1, 2) \quad (4)$$

and

$$\kappa_{12} \equiv \frac{1}{\hbar^2} \mathbf{d}_{01}^* \cdot \hat{\mathbf{C}}(\mathbf{r}_0, \mathbf{r}_0, \omega_0) \cdot \mathbf{d}_{02}. \quad (5)$$

The coefficient  $\gamma_i$  characterizes the transition  $|0\rangle$  to  $|i\rangle$ , and is called the *decay rate*; the coefficient  $\kappa_{12}$  characterizes a

cross-coupling between the states  $|1\rangle$  and  $|2\rangle$  (and  $\kappa_{21} = \kappa_{12}^*$ ). These coefficients are defined in Eqs. (4) and (5) in terms of the *correlation tensor*  $\hat{\mathbf{C}}$ :

$$\hat{\mathbf{C}}(\mathbf{r}, \mathbf{r}', \omega) \equiv \int_{-\infty}^{+\infty} d\tau \langle \hat{\mathbf{E}}_v^{(+)}(\mathbf{r}, \tau) \hat{\mathbf{E}}_v^{(-)}(\mathbf{r}', 0) \rangle e^{i\omega\tau}, \quad (6)$$

where the bracket indicates an ensemble average:

$$\langle \hat{\mathbf{E}}_v^{(+)}(\mathbf{r}, \tau) \hat{\mathbf{E}}_v^{(-)}(\mathbf{r}', 0) \rangle \equiv \text{Tr}_e[\rho_e(0) \hat{\mathbf{E}}_v^{(+)}(\mathbf{r}, \tau) \hat{\mathbf{E}}_v^{(-)}(\mathbf{r}', 0)]$$

(see the Appendix). This correlation tensor characterizes the amplitude of the *fluctuations* of the electric field in the vacuum state, which contain all the information about the dynamics of the system since, once they are known, the dynamics of the atom given by Eq. (3) can in principle be solved.

We now integrate Eq. (3) for an atom initially prepared in the excited state corresponding to the following initial conditions at  $t = 0$ :  $\rho_{00}(0) = 1$ ,  $\rho_{11}(0) = \rho_{22}(0) = 0$ , and  $\rho_{ij}(0) = 0$  for  $j \neq i$ , where  $\rho_{ii}(t)$  is the atomic population in the state  $|i\rangle$  and  $\rho_{ij}(t)$  is the atomic coherence between the states  $|i\rangle$  and  $|j\rangle$ . For the steady state ( $t \rightarrow \infty$ ), we find, for the atomic populations, that  $\rho_{00}(\infty) = 0$  and

$$\rho_{ii}(\infty) = \frac{\gamma_i}{\gamma_1 + \gamma_2} \quad (i = 1, 2), \quad (7)$$

and, for the atomic coherences, that  $\rho_{10}(t) = \rho_{20}(t) = 0$  ( $\forall t$ ) and (using the fact that  $\kappa_{21}^* = \kappa_{12}$ )

$$\rho_{12}(\infty) = \frac{\kappa_{12}}{\gamma_1 + \gamma_2}. \quad (8)$$

While the result in Eq. (7) simply shows that the populations in the steady state are in a probabilistic distribution either in state  $|1\rangle$  or  $|2\rangle$ , the result in Eq. (8) for the coherence  $\rho_{12}$  is more surprising: it reveals that a coherence between the two ground states can be induced by *spontaneous emission*, i.e., *without* an external field, while to date it was thought that a coherence between the two ground states required an external coherent field such as a laser field ([17], Chap. 3). Furthermore, because it involves ground states, this coherence has in principle a long lifetime, in the millisecond range for NV centers at room temperature [21], and in the order of seconds for cold atom systems where collisions are suppressed. Therefore, we have simply ignored the relaxation term of  $\rho_{12}$  in Eq. (3), which is supposed to be of much longer time than the coherence involving the excited state.

The detection of the coherence  $\rho_{12}$  in NV centers can be performed following the protocols discussed in [18]: A magnetic field bias is applied to lift the degeneracy between the two ground states  $|\pm 1\rangle$ . It allows one to address separately the transitions  $|\pm 1\rangle \rightarrow |0\rangle$  with two microwave fields, where  $|0\rangle$  is another magnetic sublevel. The presence of coherence between the state  $|\pm 1\rangle$  results in a phase-sensitive transfer to  $|0\rangle$ . Finally, the population of  $|0\rangle$  is probed optically using a cycling transition with an auxiliary excited state  $|E_y\rangle$  (see [18]). With cold atomic ensembles, a similar method could be employed using the hyperfine structure of the ground state of alkali-metal atoms. In this case, the coherence  $\rho_{12}$  is generated between two states within one Zeeman manifold. Then, two radio-frequency fields perform a phase-sensitive transfer to a state belonging to another Zeeman manifold. Finally, the population of this last state is optically measured.

## B. Anisotropic quantum vacuum

We will now find the conditions for the existence of the long-lifetime coherence of Eq. (8). For that, we first use the *fluctuation-dissipation theorem* at zero temperature (we do not consider the effect of the temperature, which is indeed very small when one considers an atom emitting at optical frequencies). This theorem links the correlation tensor  $\hat{\mathbf{C}}$  of Eq. (6), which we recall characterizes the vacuum electric-field *fluctuations*, to the imaginary part of the Green tensor  $\hat{\mathbf{G}}$ , which describes the *dissipation* of the electric energy, as [11]

$$\hat{\mathbf{C}}(\mathbf{r}, \mathbf{r}', \omega) = \frac{2\hbar\omega^2}{\epsilon_0 c^2} \text{Im}[\hat{\mathbf{G}}(\mathbf{r}, \mathbf{r}', \omega)]. \quad (9)$$

The fluctuation-dissipation theorem shows that the amplitude of the fluctuations is known once the imaginary part of the Green tensor has been calculated. Making use of it, the coefficients  $\gamma_i$  [Eq. (4)] and  $\kappa_{12}$  [Eq. (5)] can be expressed in term of the Green tensor as

$$\gamma_i = \frac{2\omega_0^2}{\hbar\epsilon_0 c^2} \mathbf{d}_{0i}^* \cdot \text{Im}[\hat{\mathbf{G}}(\mathbf{r}_0, \mathbf{r}_0, \omega_0)] \cdot \mathbf{d}_{0i} \quad (10)$$

and

$$\kappa_{12} = \frac{2\omega_0^2}{\hbar\epsilon_0 c^2} \mathbf{d}_{01}^* \cdot \text{Im}[\hat{\mathbf{G}}(\mathbf{r}_0, \mathbf{r}_0, \omega_0)] \cdot \mathbf{d}_{02}. \quad (11)$$

Next, we express the Green tensor and the dipole moments appearing in Eqs. (10) and (11) in the Cartesian basis  $(\vec{x}, \vec{y}, \vec{z})$  (we recall that a static magnetic field is applied along the  $\vec{z}$  direction, defining the quantization axis). Equation (8) can then be recast in the following form (using the fact that  $G_{yx} = G_{xy}$ ):

$$\rho_{12}(\infty) = \underbrace{\frac{d_{01}d_{02}}{d_{01}^2 + d_{02}^2}}_R \times \underbrace{\frac{\text{Im}[G_{xx} - G_{yy}] - i2\text{Im}[G_{xy}]}{\text{Im}[G_{xx} + G_{yy}]}_A, \quad (12)$$

where the Green tensor Cartesian components have to be evaluated at the position of the quantum emitter  $\mathbf{r}_0$  and at the transition frequency  $\omega_0$ .

One immediately remarks that in the usual isotropic vacuum  $G_{xx} = G_{yy}$  and  $G_{xy} = 0$ , and Eq. (12) predicts null coherence. Therefore, in order to generate coherence, the vacuum has to be *anisotropic*. A similar result was first put forward by Agarwal in [11] for a  $V$  configuration, where he predicted a coherent population transfer between the two orthogonal excited states in an AQV.

To quantify the anisotropy, the coherence in Eq. (12) can be written as a product of two terms: the coefficients  $R$  and  $A$ , characterizing the quantum emitter on one hand, and the vacuum anisotropy on the other hand.  $R$  reaches its maximum value of 0.5 when the two dipole moment amplitudes are equal ( $d_{01} = d_{02}$ ). The coefficient  $A$  (referred to hereafter as the “anisotropy”), in its general form, is a complex quantity, and depends on the em environment which is completely characterized by  $\hat{\mathbf{G}}$ . In this paper, we will only consider situations where  $G_{xy} = 0$  (which will be justified later), so from now on  $A$  will be considered as a real quantity and takes the form of a *visibility* with extremum values  $\pm 1$ . Therefore the extrema of the coherence are  $\rho_{12}(\infty) = \pm 1/2$ .

### C. Interpretation in terms of dressed states

In situations where the coherence is extremum, the atomic density matrix, after spontaneous emission, reads in the basis of the two ground states  $\{|1\rangle, |2\rangle\}$ :  $\rho(\infty) = \frac{1}{2} \begin{bmatrix} 1 & \pm 1 \\ \pm 1 & 1 \end{bmatrix}$ , which corresponds to a pure state. This is in stark contrast with the *isotropic* vacuum where spontaneous emission produces a statistical mixture with a reduced density matrix  $\rho(\infty) = \frac{1}{2} \mathbb{I}$ .

One can interpret this in terms of the dressed states of the system (atom plus field). Everything happens as if, after the emission of a photon ( $t \rightarrow \infty$ ), the atom-field “dressed state” is

$$|\psi(\infty)\rangle = \frac{1}{\sqrt{d_{01}^2 + d_{02}^2}} \frac{1}{\sqrt{\text{Im}(G_{xx}) + \text{Im}(G_{yy})}} \\ \times \{d_{01} |1\rangle \otimes [\sqrt{\text{Im}(G_{xx})} |X\rangle + i\sqrt{\text{Im}(G_{yy})} |Y\rangle] \\ + d_{02} |2\rangle \otimes [\sqrt{\text{Im}(G_{xx})} |X\rangle - i\sqrt{\text{Im}(G_{yy})} |Y\rangle]\}, \quad (13)$$

where  $|X\rangle = 1/\sqrt{2}(|\sigma^+\rangle + |\sigma^-\rangle)$  [respectively,  $|Y\rangle = 1/\sqrt{2}i(|\sigma^+\rangle - |\sigma^-\rangle)$ ] represents the state of photons emitted with a linear polarization along  $\vec{x}$  [respectively,  $\vec{y}$ ]. Indeed, when tracing over the emitted photon, this fully agrees with Eq. (12), and one also finds that  $\rho_{ii}(\infty) = d_{0i}^2/(d_{01}^2 + d_{02}^2) = \gamma_i/(\gamma_1 + \gamma_2)$  (for  $i = 1, 2$ ), in agreement with Eq. (7).

In isotropic vacuum, and when the two ground states are equally weighted ( $d_{01} = d_{02}$ ,  $\gamma_1 = \gamma_2$ ), it is well known that the atom and the emitted photons are fully entangled [22]: at the end of the decay process, the atom-field state is of the form

$$|\psi(\infty)\rangle = \frac{1}{\sqrt{2}}(|1\rangle \otimes |\sigma^+\rangle + |2\rangle \otimes |\sigma^-\rangle). \quad (14)$$

The reduced state of each subsystem (atom and field as well) is thus fully incoherent, which explains why in isotropic vacuum we obtain a reduced density matrix  $\rho(\infty) = \frac{1}{2} \mathbb{I}$ . It also explains why in order to observe quantum beats between the emitted photons in the vacuum a  $V$  transition is necessary, and no quantum beats will appear in the case of a  $\Lambda$  transition (see [22], Chap. 1.4).

However, if the back reaction of the environment fully eliminates the  $X$  component of the polarization [i.e., then  $\text{Im}(G_{xx}) = 0$ , which can be achieved with a metasurface as we will see later], the atom-field state at the end of the decay process is of the form

$$|\psi(\infty)\rangle = \frac{1}{\sqrt{2}}(|1\rangle - |2\rangle) \otimes \frac{1}{\sqrt{2}i}(|\sigma^+\rangle - |\sigma^-\rangle). \quad (15)$$

This atom-field state is factorizable (as it is the case for a  $V$  transition in isotropic vacuum), but here the atom is in a coherent superposition of ground states (whereas for a  $V$  transition it is the photon which is in a coherent superposition of two different modes). This means that the reduced density matrix of each subsystem is a pure state. In particular, we obtain here an atomic density matrix  $\rho(\infty)$  equal to the one-dimensional (1D) projector:  $\rho(\infty) = \frac{1}{2} \begin{bmatrix} 1 & -1 \\ -1 & 1 \end{bmatrix}$ .

The environment can thus act as a quantum eraser which erases the entanglement between the atom and the field

(emitted photon). According to the general complementary relation between the entanglement of a system with its environment and the degree of coherence of the reduced density matrix of this system [23,24], the isotropic vacuum corresponds to the situation where atom and field are maximally entangled so that their coherence is minimal (zero); in contrast, if the environment acts exactly as a polarization filter that destroys linear polarization along  $\vec{x}$ , it also destroys the correlations (entanglement) between the emitted photon and the two ground states, which fully restores the atomic coherence. In realistic situations (as we will see in Sec. III), only partial coherence is achieved, as an intermediary between these two extreme cases (isotropic vacuum and ideal anisotropic vacuum).

### III. METASURFACE DESIGNS

Vacuum anisotropy appears naturally in the near field of a material media (see, e.g., [25]). For instance, anisotropic suppression of spontaneous emission of atoms located between two close mirrors has been reported by Jhe *et al.* [26]. Anisotropy of Casimir-Polder interactions between atoms and planar surfaces has also been investigated [27] leading to atomic level mixing [28]. Resonant nanostructures are also known to show important discrepancies between  $\text{Im}(G_{xx})$  and  $\text{Im}(G_{yy})$  in the near field of, for example, metallic nanodisks [29], nanoparticles [30,31], or graphene [32]. Interestingly, although near-field interactions can dramatically enhance the QE spontaneous emission because of large  $\text{Im}(G_{ii})$  values, they are not better than far-field interactions for producing an optimum value of the anisotropy  $A$  in Eq. (12).

Metasurfaces acting as a spherical mirror with polarization-dependent responses have been proposed to create anisotropic vacuum [7,8] in the far field. As a first example, looking at Eq. (12), one can consider the ideal case of a metasurface that perfectly reflects back to the QE half of its own emission only at a particular polarization, say the  $x$  component, leading to perfect destructive interferences and thus  $\text{Im}[G_{xx}(\mathbf{r}_0, \mathbf{r}_0, \omega_0)] = 0$ . Considering that the other polarization component (the  $y$  component) is not affected and thus  $\text{Im}[G_{yy}(\mathbf{r}_0, \mathbf{r}_0, \omega_0)] = \gamma_0/2$ , its value in vacuum, such a metasurface might lead to an optimum anisotropy  $A = -1$ . This was the strategy followed in [7] in order to induce the coherent population transfer predicted in [11] for a  $V$  configuration.

A metasurface can alternatively be designed as acting on circular polarizations. To clarify this, instead of expressing the quantities appearing in Eqs. (10) and (11) in Cartesian coordinates [as done to obtain Eq. (12)], let us express the Green tensor and dipole moments in the spherical basis ( $\vec{\varepsilon}_+$ ,  $\vec{\varepsilon}_-$ ,  $\vec{\varepsilon}_0$ ), where  $\vec{\varepsilon}_\pm = (\vec{x} \pm i\vec{y})/\sqrt{2}$  and  $\vec{\varepsilon}_0 = \vec{z}$ . Then, by plugging these expressions into Eq. (8), one finds the following expression for the coherence:

$$\rho_{12}(\infty) = \underbrace{\frac{d_{01}d_{02}}{d_{01}^2 + d_{02}^2}}_R \times \underbrace{\frac{\text{Im}(G_{+-})}{\text{Im}(G_{++})}}_A, \quad (16)$$

where the Green tensor spherical components have again to be evaluated at the position of the quantum emitter  $\mathbf{r}_0$  and at the transition frequency  $\omega_0$ . This expression is

equivalent to Eq. (12), since the Green tensor components in the different bases verify the following relations:  $G_{+-} = \frac{1}{2}(G_{xx} - G_{yy} - i2G_{xy})$  and  $G_{++} = G_{--} = \frac{1}{2}(G_{xx} + G_{yy})$ . The form of Eq. (16) suggests that a metasurface that mixes the circular polarizations  $\sigma^+$  and  $\sigma^-$ , thus leading to a non-null cross-term  $\text{Im}[G_{+-}(\mathbf{r}_0, \mathbf{r}_0, \omega_0)] \neq 0$ , might create a coherence. Ideally, if the metasurface totally inverts the absolute rotation direction of the electric field with respect to that of the incident circularly polarized one, one will have  $\text{Im}[G_{+-}(\mathbf{r}_0, \mathbf{r}_0, \omega_0)] = \text{Im}[G_{++}(\mathbf{r}_0, \mathbf{r}_0, \omega_0)]$ , and thus a maximum anisotropy  $A = 1$ . This strategy was employed in [8] in order to induce a coherence between the two excited states in a  $V$  configuration.

In this section, we present the two designs of the metasurface discussed in the above examples, we compare their performances, and we assess the value of the induced coherence, taking into account the limitations of such designs. But first of all, we present in Sec. III A the general approach used to make the designs.

### A. Phase-mapping approach

The problem considered here is the interaction between a planar (meta)surface and an electric dipole source of emission wavelength  $\lambda_0$  located at a distance  $d$  above the surface. For an emitter located at remote distances (in the far field  $d \gg \lambda_0$ ), the interaction will be efficient only if the metasurface is able to reflect and focus back the light originating from the ‘‘point’’ dipole source. Thus, the metasurface must be optically equivalent to a spherical mirror of focal length  $f = d/2$ , by producing the following spherical phase profile:

$$\varphi(\mathbf{r}) = \pi - 2k_0|\mathbf{r} - \mathbf{r}_0| \pmod{2\pi}, \quad (17)$$

where  $k_0 = 2\pi/\lambda_0$ ,  $\mathbf{r}$  denotes the coordinates of the points of the metasurface, and  $\mathbf{r}_0$  denotes the coordinates of the QE.

We parametrize the problem as follows: the points  $\mathbf{r}$  lie in the plane  $z = 0$ :  $\mathbf{r} = (x, y, 0)$ , and  $\mathbf{r}_0 = (0, 0, d)$ . In other words, the phase accumulated through propagation should be compensated in each point  $\mathbf{r}$  of the flat metasurface—hence the minus sign in Eq. (17)—by a phase shift corresponding to the phase profile given in Eq. (17). Such metasurfaces create interferences and a diffraction limited spot (at the position of the QE  $\mathbf{r}_0$ ), and are the equivalent in reflection of *metalenses* [9,10]. They can be implemented using metallic subwavelength reflect arrays, made of a metallic mirror, a dielectric spacer, and subwavelength structures (also called *meta-atoms* or nanoantennas) patterned on top (see Fig. 2).

By carefully choosing and positioning the meta-atoms, the metasurface can induce local phase shifts that mimic the spherical phase profile given by Eq. (17). This is the principle of the *phase-mapping approach*. Obviously, each design is specific for a couple of parameters  $\{\lambda_0, d\}$ , so a modification of one of these parameters leads to a new design. Good power reflectances were reported for such metasurfaces at normal incidence: about 80% for gold reflect arrays in the range 700–1100 nm [7,33–35] and up to 90% for silver reflect arrays around 640–670 nm [8,36].

In order to design the metasurface, one usually extrapolates its properties from the computations of an *infinite periodic grating*. Such an approach assumes that *locally* the properties

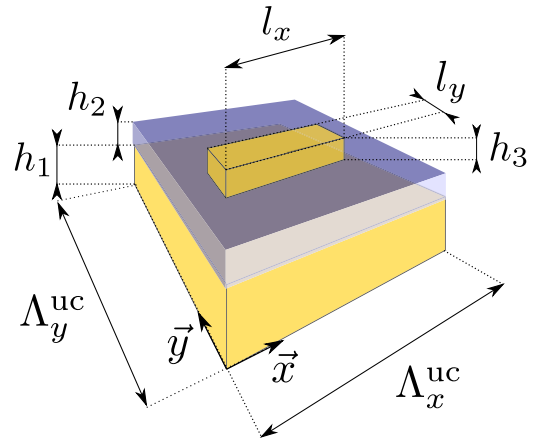


FIG. 2. Unit cell of a reflect-array metasurface made of a metallic mirror of thickness  $h_1$ , a dielectric spacer of thickness  $h_2$ , and a rectangular nanoantenna of dimensions  $l_x \times l_y$  and of thickness  $h_3$ . The dimensions of the unit cell are  $\Lambda_x^{\text{uc}} \times \Lambda_y^{\text{uc}}$ .

of the metasurface are close to those of a periodic grating, which is valid if the meta-atoms behave independently [9] and is referred to as the *local-periodicity approach*. Adopting this approach, all the numerical simulations in this paper are done using the open-source RETICOLO software for grating analysis [37], which implements a frequency-domain modal method known as the rigorous coupled wave analysis (RCWA) [38–41]. Since it is a Fourier modal method, we specify for each simulation the number of Fourier modes retained for the computation (which are given for the direction  $\vec{x}$ , and we use the same number of modes for the direction  $\vec{y}$ ). Moreover, all the meta-atoms considered here are nanorods that respect a mirror symmetry, and therefore throughout this paper  $G_{xy} = 0$  [42].

In Secs. III B and III C, we present two designs aiming at creating the coherence in the QE, and we characterize their performances.

### B. Design based on resonant-phase delays

In this section, we design the metasurface discussed in the first example above—inspired from Eq. (12)—that must have the following optical properties.

(i) The metasurface acts as a spherical mirror *only* for a linearly polarized light along  $\vec{x}$ , resulting in  $G_{xx}(\mathbf{r}_0, \mathbf{r}_0, \omega_0) = 0$  (destructive interferences).

(ii) The metasurface acts as a planar mirror for a linearly polarized light along  $\vec{y}$ , so  $G_{yy}(\mathbf{r}_0, \mathbf{r}_0, \omega_0)$  is untouched.

Such a metasurface can be built from anisotropic resonant nanoantennas, using, for example, metallic nanorods (like the one represented in Fig. 2) with varying lengths along  $\vec{x}$ , in order to tune the resonance and to induce different phase shifts or *resonant-phase delays* on a  $x$ -polarized light that reproduce the spherical phase profile of Eq. (17), and the same width along  $\vec{y}$ , in order to induce a constant phase shift on a  $y$ -polarized light that produces a flat phase profile [7,33,34].

For the simulations, we consider a two-dimensional (2D) grating made of unit cells of the type presented in Fig. 2 with lateral dimensions of  $\Lambda_x^{\text{uc}} \times \Lambda_y^{\text{uc}} = 300 \times 150$  nm, and

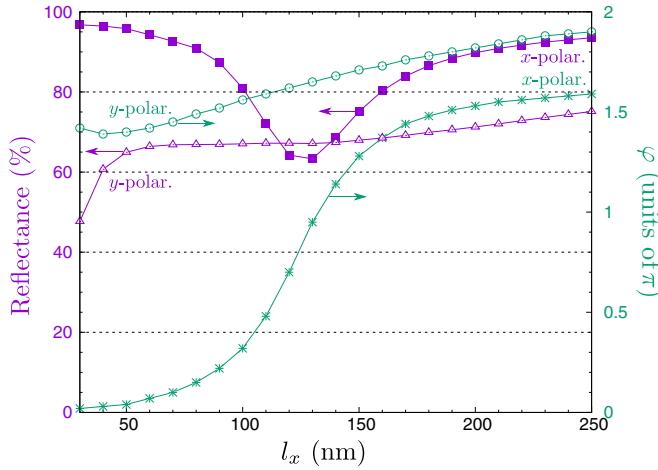


FIG. 3. Power reflectance (in purple) and phase shift  $\varphi$  (in green) of an incident  $x$ -polarized (respectively,  $y$ -polarized) wave as a function of the length  $l_x$  of the nanoantennas, computed for a 2D grating (see main text). The symbols represent the simulated points, and the solid lines are guides to the eyes. The dotted black lines are spaced by  $2\pi/5$ . The number of Fourier modes used for the simulations is 30.

made of a gold mirror and a dielectric film of  $\text{SiO}_2$  with respective thicknesses  $h_1 = 130$  nm and  $h_2 = 50$  nm, and a gold nanorod patterned on top with fixed width  $l_y = 100$  nm and thickness  $h_3 = 30$  nm. The wavelength is chosen at  $\lambda_0 = 852$  nm, which corresponds to the  $D_2$  line of cesium atom. At this wavelength, the refractive indices are  $n = 0.16 + i5.34$  for gold and  $n = 1.45$  for  $\text{SiO}_2$ . In Fig. 3, we computed the phase shifts (in green) and the efficiencies in reflection (in purple) of such a 2D grating, for incident  $x$ - and  $y$ -polarized waves at normal incidence, as a function of the length  $l_x$  of the nanorod. One can see that the phase shift induced on a  $x$ -polarized wave (green crosses) spans over  $8\pi/5$  ( $1.6\pi$ ), which corresponds to  $4/5$  of the  $2\pi$  phase space, while the phase shift induced on a  $y$ -polarized wave (green circles) is rather flat. We can therefore choose five nanoantennas to sample the entire phase space of  $2\pi$ , with respective phase shifts of  $0$ ,  $2\pi/5$ ,  $4\pi/5$ ,  $6\pi/5$ , and  $8\pi/5$  (intersection with the dotted black lines spaced by  $2\pi/5$ ; see dimensions in Table I). Moreover, the power reflectance of the  $x$ -polarized wave (purple squares), which is the only one that matters, is relatively good, remaining between 63 and 97%, the losses being due to absorption by the metal (we check that the gold mirror is thick enough and that there is no transmission loss).

TABLE I. Nanoantenna dimensions for sampling the phase space from zero to  $2\pi$ .

Nanoantenna	$l_x$ (nm)	$l_y$ (nm)
No. 1	30	100
No. 2	105	100
No. 3	125	100
No. 4	145	100
No. 5	250	100

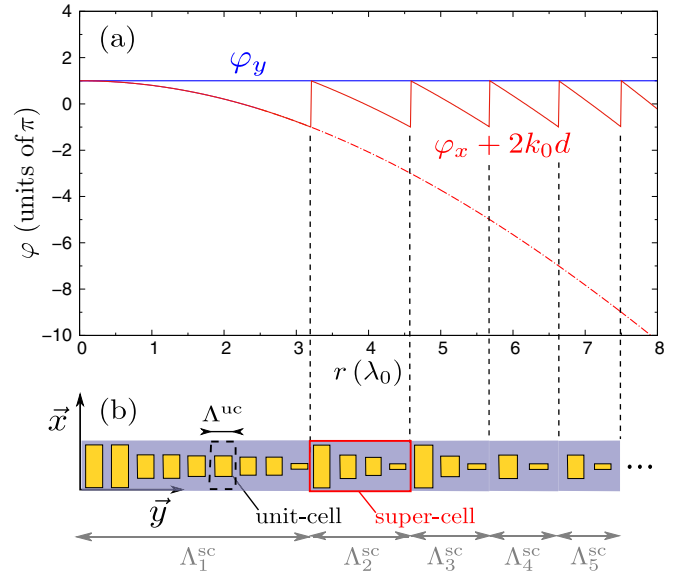


FIG. 4. Illustration of the phase-mapping approach for the 1D design of the resonant-phase delay metasurface. (a) Phase profiles to be encoded by the metasurface: the wrapped (respectively, unwrapped) spherical phase profile  $\varphi_x$  of Eq. (17) (respectively, red full line) (respectively, red dashed line) desired for the  $x$ -polarization, and the flat phase profile  $\varphi_y$  (blue line) desired for the  $y$ -polarization, starting from the center of the metasurface at  $r = 0$ . (b) Corresponding nanoantennas to encode the desired phase shifts  $\varphi_x$  and  $\varphi_y$ . The unit cells of length  $\Lambda^{\text{uc}}$  (black dashed box) containing the nanoantennas are encompassed into supercells of length  $\Lambda^{\text{sc}}$  (red box), spanning the  $2\pi$  phase space.

The design of the metasurface is achieved after combining these five nanoantennas while employing the following rules: All nanoantennas must be parallel (the varying length  $l_x$  always oriented along the  $\vec{x}$  axis), and patterned after Eq. (17) according to the phase-mapping approach. This design is illustrated “in 1D” in Fig. 4: In Fig. 4(a), we plot the ideal unwrapped (respectively, wrapped) phase profile of Eq. (17) of a  $x$ -polarized wave in dashed red (respectively, full red), and the ideal flat phase profile of a  $y$ -polarized wave in blue, starting from the center of the metasurface at  $r = 0$ ; in Fig. 4(a), we represent a slice of the metasurface where the nanoantennas are distributed into supercells (one of them is highlighted in the red box) that sample the  $2\pi$  phase space, mimicking the phase profiles of Fig. 4(a). The size of the supercells is maximum at the center of the metasurface, and progressively decreases with distance from the center because the spherical phase profile varies more rapidly.

In addition to the absorption losses, the sampling of the phase by *discrete* elements in the phase-mapping approach also limits the performances of the metasurface (one talks about *discretization losses*). In order to assess these discretization losses, we compute the performances in the canonical case of a *linear-phase gradient metasurface* [33,34], which behaves as a *blazed grating* that diffracts entirely into the diffraction order  $m = -1$  only for an incident  $x$ -polarized wave. Such a gradient metasurface is made of the same supercell containing nanoantennas that sample the phase regularly

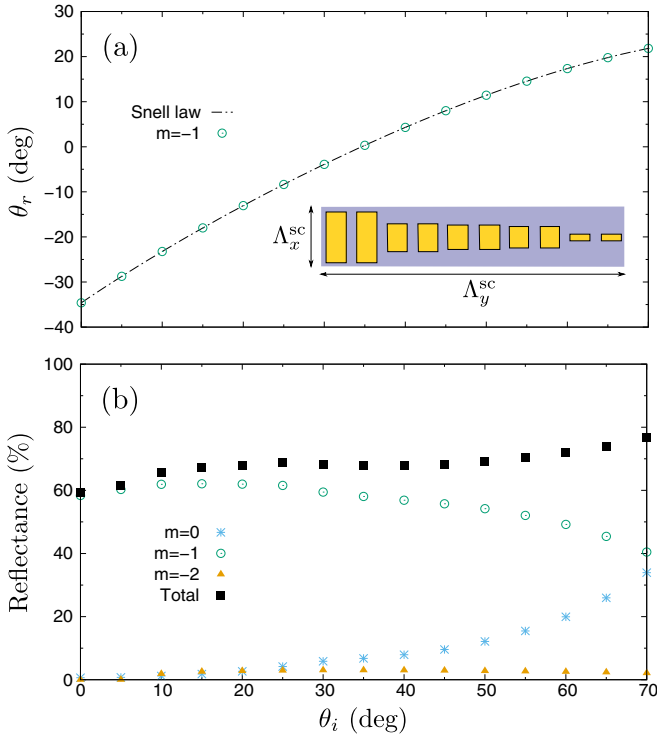


FIG. 5. Diffraction performances of a linear-phase gradient metasurface. The inset shows a supercell of the gradient metasurface of size  $\Lambda_x^{\text{sc}} \times \Lambda_y^{\text{sc}}$  (see main text). (a) Reflection angle  $\theta_r$  in the diffracted order  $m = -1$  of an incident plane wave polarized along  $\vec{x}$  as a function of the incident angle  $\theta_i$  (green circles). The generalized Snell's law of reflection [Eq. (18)] is also plotted (black dashed line). (b) Power reflectance in the diffracted orders  $m = 0, -1, -2$  (blue stars, green circles, and orange triangles, respectively) and total reflection efficiency (black squares) of an incident plane wave polarized along  $\vec{x}$  as a function of the incident angle  $\theta_i$ . The number of Fourier modes used to compute the reflectance is 30.

from  $2\pi$  to zero (and from zero to  $2\pi$  to diffract into the order  $m = +1$ ), repeated with periodic boundary conditions.

For the simulations, we consider a linear-phase gradient metasurface made of supercells of dimensions  $\Lambda_x^{\text{sc}} \times \Lambda_y^{\text{sc}} = 300 \times 1500$  nm, in which the five nanoantennas previously selected are embedded into unit cells, with the same dimensions as previously, and repeated twice [see inset in Fig. 5(a)]. The working wavelength is still 852 nm, as previously. The angle of the diffracted order  $m = -1$  (reflection angle  $\theta_r$ ) is given in terms of the angle of the incident wave (incident angle  $\theta_i$ ) by the generalized Snell law of reflection [10]:

$$\sin(\theta_r) = \sin(\theta_i) + \frac{\lambda_0}{2\pi} \frac{\partial \varphi}{\partial y}, \quad (18)$$

where in our case  $\partial \varphi / \partial y = -2\pi / \Lambda_y^{\text{sc}}$  with  $\Lambda_y^{\text{sc}} = 1500$  nm. We check that we perfectly recover this law in Fig. 5(a) for an incident  $x$ -polarized wave. Thus, one can see that the diffraction angle is the same either for a periodic blazed grating or for a smooth linear-gradient metasurface, because it only depends on the period and not on the underlying structure [43].

In Fig. 5(b), we computed the power reflectance of the diffracted order  $m = -1$  for an incident  $x$ -polarized wave (green circles) as a function of the incident angle  $\theta_i$ , and

TABLE II. Characteristics of the supercells of the metasurface shown in Fig. 4, labeled by integer  $n = 1, 2, 3, 4, 5$  (starting from the center of the metasurface): length  $\Lambda^{\text{sc}}$  (in units of  $\lambda_0$ ), number of unit cells  $N$  per supercell, incident angle  $\theta_i$  of the light impinging the supercell, and power reflectance in the order  $m = -1$  (computed for a linear-phase gradient metasurface made of the supercell and at the incident angle  $\theta_i$ ). The number of Fourier modes used to compute the reflectance is 30.

Supercell $n$	$\Lambda^{\text{sc}} (\lambda_0)$	$N$	$\theta_i (^\circ)$	Reflectance (%)
1	3.17	9	0	60
2	1.41	4	17.6	55
3	1.06	3	24.6	50
4	0.94	2	29.4	30
5	0.82	2	33.3	30
$\infty$	0.50	1	90.0	0

compare it with other dominant orders  $m = 0$  (blue stars) and  $m = -2$  (orange triangles). The total power reflectance is also shown (dark squares). First, the total power reflectance, which varies between 59 and 77%, reveals absorption losses between 23 and 41%, depending on the incident angle. Second, one can see that the reflectance of the order  $m = -1$  is about 60% for incident angles  $\theta_i$  up to  $30^\circ$ , and then decreases until 40% for an incident angle of  $70^\circ$ , while mostly the reflectance of the order  $m = 0$  increases. This reveals that while the reflectance into a given order depends on the incident angle  $\theta_i$  it is relatively robust with the variations of  $\theta_i$  (1/3 decrease of the reflectance of the order  $m = -1$  over  $70^\circ$ ).

The final metasurface is more complex than a linear-phase gradient metasurface since it is made of supercells of different sizes. One can show from Eq. (17) that the largest supercell starts at  $r = 0$  (at the center of the metasurface) and has a length of  $\Lambda_{\text{max}}^{\text{sc}} = \sqrt{d\lambda_0}$ , and that the length of the next supercells quickly converges towards the minimum length of  $\Lambda_{\text{min}}^{\text{sc}} = \lambda_0/2$ . In Table II, for a design working at  $\{\lambda_0 = 852 \text{ nm}, d = 10\lambda_0\}$ , we give the length  $\Lambda^{\text{sc}}$  of the first five supercells represented in Fig. 4(b) (and labeled  $n = 1, \dots, 5$  starting from the center) and the number of unit cells  $N$  per supercell, considering a unit cell of fixed length  $\Lambda^{\text{uc}} = 300$  nm ( $\approx 0.35\lambda_0$ ). One can see that the number of unit cells—and therefore of nanoantennas—quickly drops from 9 (first supercell) to 2 (fourth supercell). Consequently, the sampling of the phase deteriorates, leading to higher discretization losses.

We computed in Table II the power reflectance of the order  $m = -1$  (for an incident  $x$ -polarized wave) for different linear-phase gradient metasurfaces made of these supercells, and taking into account the incident angle  $\theta_i$  (also shown) at which the light impinges the supercell in the final metasurface. One can see that the reflectance decreases as the number of unit cells per supercell decreases; in other words, the discretization losses increase.

In summary, the performances of the metasurface are reduced for two main reasons: the absorption losses and the discretization losses due to the finite number of unit cells used to sample the phase. They are better in the center of the metasurface, and deteriorate quickly when getting further from the center (or with increasing of the incident angle), which limits the numerical aperture (NA) of the metasurface.

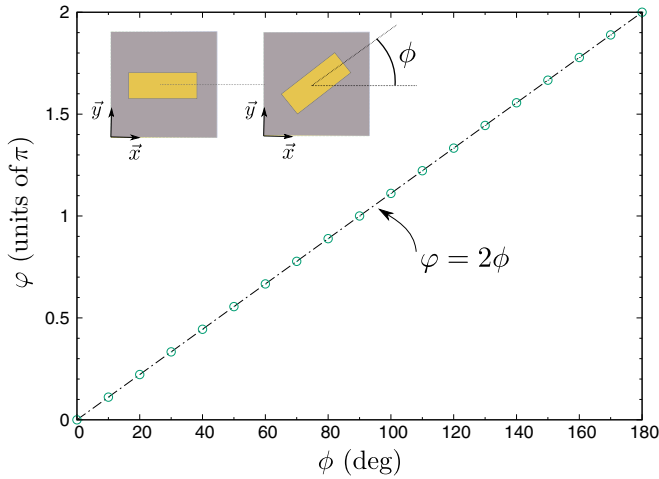


FIG. 6. Geometric phase  $\varphi$  as a function of the rotation angle  $\phi$  of the nanorods in the plane  $(\vec{x}, \vec{y})$  (see inset), computed for a 2D grating (see main text) (green circles). The analytical expression [Eq. (19)] is also plotted (black dashed line). The number of Fourier modes used to compute the geometric phase is 30.

### C. Design based on geometric phases

In this section, we design the metasurface discussed in the second example above—inspired from Eq. (16)—that must have the following properties.

- (i) The metasurface acts as a spherical mirror.
- (ii) Upon reflection, the metasurface totally inverts the absolute rotation direction of the electric field with respect to that of the incident circularly polarized one.

This inversion of the electric-field rotation can be achieved by using nanoantennas which act as half-wave plates, as the result of a phase delay of  $\pi$  between the long and short axes of the nanoantennas [35,42]. Moreover, a phase shift, called *geometric phase* or *Pancharatnam-Berry phase*, which depends on the orientation of the antenna, is acquired through this inversion, according to [44,45]

$$\varphi = 2\phi, \quad (19)$$

where  $\phi$  denotes the angle by which the antenna is rotated (see inset in Fig. 6). This phase shift is of geometric origin since it is solely due to the orientation of the nanoantenna and not to its resonance properties. Thus, the spherical phase profile can be built by mapping the orientation of the nanoantennas [Eq. (19)] into the spherical phase profile [Eq. (17)].

For the simulations, we consider a 2D grating made of unit cells of the type presented in Fig. 2 with lateral dimensions of  $\Lambda_x^{\text{UC}} \times \Lambda_y^{\text{UC}} = 300 \times 300$  nm, and made of a gold mirror and a dielectric film of  $\text{MgF}_2$  with respective thicknesses  $h_1 = 130$  nm and  $h_2 = 90$  nm, and a gold nanorod patterned on top with lateral dimensions  $l_x = 200$  nm and  $l_y = 80$  nm and thickness  $h_3 = 30$  nm, following [35,42]. The working wavelength is 852 nm, and the refractive indices are  $n = 0.16 + i5.34$  for gold and  $n = 1.37$  for  $\text{MgF}_2$ . For such a system, the phase shift for a light polarized along  $\vec{x}$  and a light polarized along  $\vec{y}$  is  $\pi$  upon reflection, at 852 nm. Thus, the system acts as a half-wave plate working in reflection.

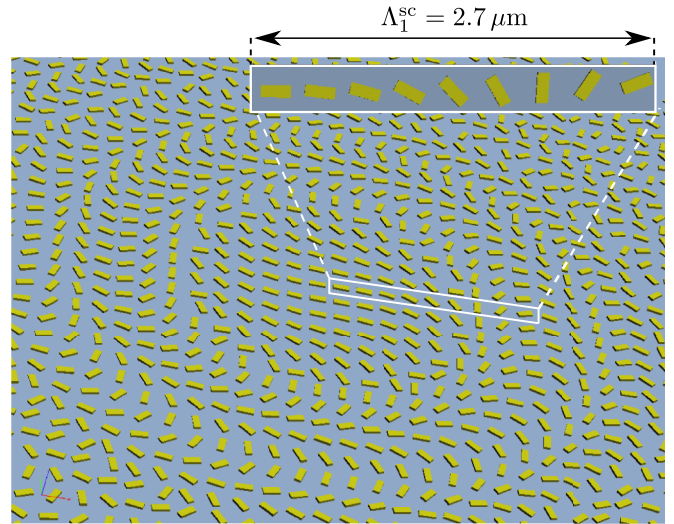


FIG. 7. Three-dimensional design of the geometric metasurface, made for a distance of the dipole source  $d = 10\lambda_0$  from the metasurface, and an emission wavelength of  $\lambda_0 = 852$  nm. The white box highlights the first supercell (starting from the center) of size  $\Lambda_1^{\text{SC}} = 2.7 \mu\text{m}$ , made of nine nanorods. This computer aided design was drawn using the software SOLIDWORKS developed by Dassault Systèmes.

We check in Fig. 6 that we recover the behavior of Eq. (19) (shown in dashed black line) by simulating the phase shift induced by a periodic grating of such nanoantennas all rotated by the same angle  $\phi$  (green circles). We show in Fig. 7 the three-dimensional drawing of such a metasurface working at  $\{\lambda_0 = 852 \text{ nm}, d = 10\lambda_0\}$ . In this figure, we also highlight the first supercell (white box) starting from the center of the metasurface.

Next, in Fig. 8, we compute the conversion efficiency of a circularly polarized  $\sigma^+$  incident wave reflected into a  $\sigma^-$  circularly polarized wave (cross-polarization reflectance) of the same 2D grating as a function of the incident angle  $\theta_i$ . One

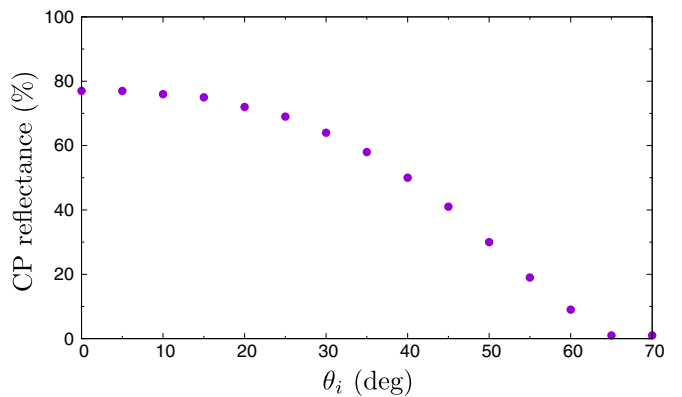


FIG. 8. Cross-polarization (CP) power reflectance, which characterizes the conversion efficiency in energy between a light circularly polarized  $\sigma^+$  and a light circularly polarized  $\sigma^-$ , as a function of the incident angle  $\theta_i$ , computed for a 2D grating (see main text). The number of Fourier modes used to compute the CP reflectance is 30.

can see that the cross-polarization power reflectance remains  $>40\%$  for  $\theta_i < 45^\circ$ . This design does not seem to be as good as the first design presented in Sec. III B, for which we recall that the power reflectance into the desired order remains  $>40\%$  up to  $\theta_i = 70^\circ$  [Fig. 5(b)]. Even though the quantities that we compare here are different, both characterize in a way the performances of the metasurface.

#### IV. ESTIMATION OF THE COHERENCE INDUCED BY THE METASURFACE

In this section, we want to assess a realistic value of the ground-state coherence  $\rho_{12}$  in the steady state [Eq. (8)] induced by a metasurface. To do so, we limit the discussion to the first design (Sec. III B), since its performances seem to be better than for the second design (Sec. III C).

If the dipole moments of the  $\Lambda$  transition are equal ( $d_{01} = d_{02} = d$ ), Eq. (12) [or equivalently Eq. (16)] becomes

$$\rho_{12}(\infty) = \frac{1}{2} \times \frac{\text{Im}[G_{xx} - G_{yy}]}{\text{Im}[G_{xx} + G_{yy}]}, \quad (20)$$

where we recall that we consider  $\text{Im}[G_{xy}] = 0$  since the nanoantennas have a mirror symmetry. By noting that, for a *two-level atom* characterized by a dipole moment  $\mathbf{d}$  oriented along the  $x$  axis, the decay rate is given by [46]

$$\gamma_x = \frac{2\omega_0^2}{\hbar\epsilon_0 c^2} |\mathbf{d}|^2 \text{Im}(G_{xx}), \quad (21)$$

and similarly for an orientation along the  $y$  axis, Eq. (20) can be recast in the form

$$\rho_{12}(\infty) = \frac{1}{2} \times \frac{\gamma_x - \gamma_y}{\gamma_x + \gamma_y}. \quad (22)$$

To evaluate the coherence of Eq. (22), one could use Eq. (21) (or equivalently the expression in terms of the scattered field as in [8,36]) and numerically compute the Green tensor  $\hat{\mathbf{G}}$  (respectively, the scattered field  $\mathbf{E}_s$ ) of the metasurface at the position of the atom, which is demanding in terms of computation time.

Instead, we choose to take advantage of the analytical results available for a spherical mirror [3]. We consider that the quantity  $\gamma_y$  is not modified compared to its free-space value:  $\gamma_y = \gamma_0$ , while  $\gamma_x$  is altered since the metasurface acts as a spherical mirror for such a polarization (in the case of the first design). The alteration of  $\gamma_x$  is calculated as a function of the power reflectance  $R_x$  (the subscript is for a light polarized along  $\vec{x}$ ) and the numerical aperture NA of the metasurface using the following expression [3]:

$$\frac{\gamma_x}{\gamma_0} = 3 \int_{2\pi} \frac{d\Omega}{4\pi} \left[ 1 - \frac{|\mathbf{d} \cdot \boldsymbol{\Omega}|^2}{|\mathbf{d}|^2} \right] \times (1 - R_x), \quad (23)$$

where  $\boldsymbol{\Omega}$  is the vectorial solid angle, and for the power reflectance  $R_x$  in diffraction order  $m = -1$  we take the values given in Table II.  $R_x$  is therefore a piecewise function, where its value, for a given location on the metasurface, is given by the underlying supercell. Moreover,  $R_x = 0$  if  $\sin\theta > \text{NA}$ , which takes into account the limited size of the metasurface. Here, the use of Eq. (23), which was originally derived for a two-level atom located at the focus of a spherical mirror in [3], is justified since the metasurface acts as a spherical mirror for a dipole emitter oriented along  $\vec{x}$ . In other words,

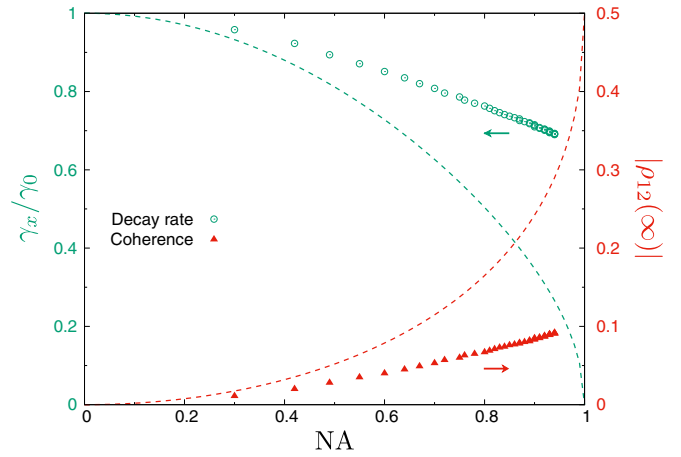


FIG. 9. Relative decay rate modifications  $\gamma_x/\gamma_0$  (green circles) and absolute coherence  $|\rho_{12}|$  (red triangles) as a function of the numerical aperture of the metasurface NA. For comparison, the relative decay rate (respectively, coherence) for an ideal spherical mirror of power reflectance  $R_x = 1$  for the  $x$  polarization only is also shown [green (respectively, red) dashed line].

the metasurface is *optically equivalent* to a spherical mirror, and has the same Green tensor or scattered field value at the position of the atom; generally speaking, since the decay rate modification depends on these quantities [see Eq. (21) in terms of the Green tensor or [8,36] in terms of the scattered field], it should then be altered in the same way as in the case of a spherical mirror, in the far-field limit. At the present time, because of limitations of the computational resources, we were not able to provide a fully numerical estimate of the absolute coherence taking into account all the details of the metasurface. Actually, although we made use of Eq. (23) out of its original context (spherical mirror), we incorporated results from numerical computations (reflectance values in Table II), which constitutes in our eyes an acceptable compromise, in between a fully numerical treatment and an educated guess.

In Fig. 9, we show the relative decay rate modifications  $\gamma_x/\gamma_0$  calculated from Eq. (23) (green circles) and the induced coherence calculated from Eq. (22) (red triangles), as a function of the numerical aperture defined as  $\text{NA} \equiv \sin\theta$ . For comparison, we also show the decay rate modifications (respectively, the induced coherence) in the case of a perfect reflective spherical mirror (power reflectance  $R_x = 1$ ) that would only reflect a polarization along  $\vec{x}$  [green dashed line (respectively, red dashed line)]. In this case, Eq. (23) can be calculated analytically and reads

$$\frac{\gamma_x}{\gamma_0} = \sqrt{1 - \text{NA}^2} \times \left( 1 - \frac{\text{NA}^2}{4} \right). \quad (24)$$

One can see that for a metasurface of  $\text{NA} = 0.7$  the decay rate  $\gamma_x$  is reduced by 20% compared to  $\gamma_0$ , with an induced coherence of  $\approx 0.05$ . Compared to the ideal case of an infinite perfect spherical mirror, this value of the coherence is about one order of magnitude smaller (0.5 for an ideal reflector with  $\text{NA} = 1$ ). Larger NA results only in a moderate improvement of the effect because of the rapid drop of the reflectance,

contrary to the ideal case. To attain near-unity efficiency in reflection, further optimizations of the antenna geometries that can take into consideration the coupling between neighboring elements are required. Several methods have been proposed including objective-first algorithms [47–49], topology optimization [50], and inverse designs [51,52], which are also applicable to improve our device efficiency notably at large deflection angles, but beyond the scope of the present paper.

## V. CONCLUSION

In this paper, we predict the creation of a long-lifetime coherence between the two ground states of a quantum emitter with a  $\Lambda$  configuration, induced by a quantum anisotropic vacuum. An AQV can be engineered over macroscopic distances by a metasurface, made of metallic subwavelength reflect arrays and having a polarization-dependent response. We proposed and designed two of such metasurfaces, based on the phase-mapping approach, using two different techniques: *resonant phase delays* and *geometric phases*. We quantify the efficiency of these metasurfaces to redirect the light on the quantum emitter, located at remote distances, by taking into account the limitations on the numerical aperture due to the phase-mapping approach. Based on the exact results available for a spherical mirror, we estimate a redirection of the light of about 20% for a numerical aperture of 0.7, leading to a coherence of 0.05, which is one order of magnitude smaller than in the ideal case of an infinite and perfect reflector. Nevertheless, due to the long lifetime of this coherence involving the ground states in a  $\Lambda$  transition, this system allows for high-resolution experiments, and this effect should be observable using the current state-of-art NV-center experimental platform [18]. Detecting this coherence would represent an experimental demonstration of the effect of the anisotropy of vacuum on quantum emitters at remote distances. In addition, this experiment would be a test of quantum electrodynamics, in a counterintuitive regime where coherence is driven by relaxation processes and vacuum fluctuations. Moreover, such an experimental demonstration would also pave the way for controlling interactions between several quantum emitters by the means of metasurfaces, which ultimately could be used to generate entanglement for quantum technology applications in a new paradigm [16,36].

## ACKNOWLEDGMENTS

The authors wish to thank Gabriel Hétet, Guanghui Yuan, Giorgio Adamo, Weibo Gao, and Martial Ducloy for fruitful discussions. E.L. thanks Institut Fresnel (via Fonds pour la Science 2018) and Nanyang Technological University for supporting his stay in Singapore. This work is supported by the Singapore Ministry of Education Academic Research Fund Tier 3 Grant No. MOE2016-T3-1-006(S).

## APPENDIX: MASTER EQUATION DERIVATION

In this Appendix, we present the master equation framework, closely following [19] Chap. 5.6 and [20] Chap. 1, that we used to derive the master equation [Eq. (3)] in Sec. II.

### 1. Short notations

It will be convenient for the following calculations to rewrite  $\hat{H}_I(t)$  of Eq. (1) in a more compact form:

$$\hat{H}_I(t) = \hat{\mathbf{d}}^\dagger(t) \cdot \hat{\mathbf{E}}_v^{(+)}(t) + \hat{\mathbf{d}}(t) \cdot \hat{\mathbf{E}}_v^{(-)}(t) \quad (\text{A1})$$

where  $\hat{\mathbf{d}}(t)$  and  $\hat{\mathbf{d}}^\dagger(t)$  are defined by

$$\hat{\mathbf{d}}(t) \equiv -(\mathbf{d}_{01}^* |1\rangle \langle 0| e^{-i\omega_1 t} + \mathbf{d}_{02}^* |2\rangle \langle 0| e^{-i\omega_2 t}), \quad (\text{A2})$$

$$\hat{\mathbf{d}}^\dagger(t) \equiv -(\mathbf{d}_{01} |0\rangle \langle 1| e^{i\omega_1 t} + \mathbf{d}_{02} |0\rangle \langle 2| e^{i\omega_2 t}). \quad (\text{A3})$$

Note that for clarity we dropped the label  $\mathbf{r}_0$  appearing in  $\hat{\mathbf{E}}_v^{(+)}(\mathbf{r}_0, t)$  and  $\hat{\mathbf{E}}_v^{(-)}(\mathbf{r}_0, t)$ , but one must remember that the fields are evaluated at the position of the atom  $\mathbf{r}_0$ . One must also take note that this Hamiltonian is written in the electric dipole and rotating wave approximations.

### 2. Master equation framework

In the *interaction picture*, the density matrix  $\rho_T(t)$  of the total system (atom plus environment) obeys the Schrödinger equation [19,20]

$$\frac{\partial \rho_T(t)}{\partial t} = \frac{1}{i\hbar} [\hat{H}_I(t), \rho_T(t)]. \quad (\text{A4})$$

The atomic density matrix  $\rho(t)$  is obtained by taking the trace over the degrees of freedom of the environment,  $\rho(t) = \text{Tr}_e[\rho_T(t)]$ , and therefore obeys

$$\frac{\partial \rho(t)}{\partial t} = \frac{1}{i\hbar} \text{Tr}_e[\hat{H}_I(t), \rho_T(t)]. \quad (\text{A5})$$

We formally integrate Eq. (A4),

$$\rho_T(t) = \rho_T(0) + \frac{1}{i\hbar} \int_0^t dt' [\hat{H}_I(t'), \rho_T(t')], \quad (\text{A6})$$

and substitute this expression in Eq. (A5):

$$\begin{aligned} \frac{\partial \rho(t)}{\partial t} &= \frac{1}{i\hbar} \text{Tr}_e[\hat{H}_I(t), \rho_T(0)] \\ &\quad - \frac{1}{\hbar^2} \int_0^t dt' \text{Tr}_e[\hat{H}_I(t), [\hat{H}_I(t'), \rho_T(t')]]. \end{aligned} \quad (\text{A7})$$

Assuming that  $\text{Tr}_e[\hat{H}_I(t), \rho_T(0)] = 0$ , we make the *Born approximation*:  $\rho_T(t) = \rho(t) \otimes \rho_e(0)$ , so that Eq. (A7) reduces to

$$\frac{\partial \rho(t)}{\partial t} = -\frac{1}{\hbar^2} \int_0^t dt' \text{Tr}_e[\hat{H}_I(t), [\hat{H}_I(t'), \rho_e(0) \otimes \rho(t')]]. \quad (\text{A8})$$

Next, we make the *Markov approximation* and replace  $\rho(t')$  by  $\rho(t)$  in the integrand. Therefore, we get a master equation for the atomic density matrix  $\rho(t)$  in the *Born-Markov approximation*:

$$\frac{\partial \rho(t)}{\partial t} = -\frac{1}{\hbar^2} \int_0^t dt' \text{Tr}_e[\hat{H}_I(t), [\hat{H}_I(t'), \rho_e(0) \otimes \rho(t)]] \quad (\text{A9})$$

Now, we write  $\hat{H}_I(t)$  explicitly and expand the commutators. Using the compact form Eq. (A1) in Eq. (A9) one gets

$$\begin{aligned} \frac{\partial \rho(t)}{\partial t} = & -\frac{1}{\hbar^2} \int_0^t dt' \text{Tr}_e[\hat{\mathbf{d}}^\dagger(t) \cdot \hat{\mathbf{E}}_v^{(+)}(t) + \hat{\mathbf{d}}(t) \cdot \hat{\mathbf{E}}_v^{(-)}(t), \\ & \times [\hat{\mathbf{d}}^\dagger(t') \cdot \hat{\mathbf{E}}_v^{(+)}(t') + \hat{\mathbf{d}}(t') \cdot \hat{\mathbf{E}}_v^{(-)}(t'), \rho_e(0) \otimes \rho(t)]] \end{aligned} \quad (\text{A10})$$

Expanding the commutators in Eq. (A10) gives 16 terms. Noting that the trace only acts on the field operators and on  $\rho_e(0)$ , and using the cyclic property of the trace operation and the fact that, for instance,  $\text{Tr}_e[\rho_e(0) \hat{\mathbf{E}}_v^{(+)}(t) \hat{\mathbf{E}}_v^{(-)}(t')] = \langle \hat{\mathbf{E}}_v^{(+)}(t) \hat{\mathbf{E}}_v^{(-)}(t') \rangle$ , we find

$$\begin{aligned} \frac{\partial \rho(t)}{\partial t} = & -\frac{1}{\hbar^2} \int_0^t dt' \langle \hat{\mathbf{E}}_v^{(+)}(t) \hat{\mathbf{E}}_v^{(-)}(t') \rangle [\hat{\mathbf{d}}^\dagger(t) \hat{\mathbf{d}}(t') \rho(t) - \hat{\mathbf{d}}(t') \rho(t) \hat{\mathbf{d}}^\dagger(t)] + \langle \hat{\mathbf{E}}_v^{(+)}(t') \hat{\mathbf{E}}_v^{(-)}(t) \rangle [\rho(t) \hat{\mathbf{d}}^\dagger(t') \hat{\mathbf{d}}(t) - \hat{\mathbf{d}}(t) \rho(t) \hat{\mathbf{d}}^\dagger(t')] \\ & + \langle \hat{\mathbf{E}}_v^{(-)}(t) \hat{\mathbf{E}}_v^{(+)}(t') \rangle [\hat{\mathbf{d}}(t) \hat{\mathbf{d}}^\dagger(t') \rho(t) - \hat{\mathbf{d}}^\dagger(t') \rho(t) \hat{\mathbf{d}}(t)] + \langle \hat{\mathbf{E}}_v^{(-)}(t') \hat{\mathbf{E}}_v^{(+)}(t) \rangle [\rho(t) \hat{\mathbf{d}}(t') \hat{\mathbf{d}}^\dagger(t) - \hat{\mathbf{d}}^\dagger(t) \rho(t) \hat{\mathbf{d}}(t')] \\ & + \langle \hat{\mathbf{E}}_v^{(+)}(t) \hat{\mathbf{E}}_v^{(+)}(t') \rangle [\hat{\mathbf{d}}^\dagger(t) \hat{\mathbf{d}}^\dagger(t') \rho(t) - \hat{\mathbf{d}}^\dagger(t') \rho(t) \hat{\mathbf{d}}^\dagger(t)] + \langle \hat{\mathbf{E}}_v^{(+)}(t') \hat{\mathbf{E}}_v^{(+)}(t) \rangle [\rho(t) \hat{\mathbf{d}}^\dagger(t') \hat{\mathbf{d}}^\dagger(t) - \hat{\mathbf{d}}^\dagger(t) \rho(t) \hat{\mathbf{d}}^\dagger(t')] \\ & + \langle \hat{\mathbf{E}}_v^{(-)}(t) \hat{\mathbf{E}}_v^{(-)}(t') \rangle [\hat{\mathbf{d}}(t) \hat{\mathbf{d}}(t') \rho(t) - \hat{\mathbf{d}}(t') \rho(t) \hat{\mathbf{d}}(t)] + \langle \hat{\mathbf{E}}_v^{(-)}(t') \hat{\mathbf{E}}_v^{(-)}(t) \rangle [\rho(t) \hat{\mathbf{d}}(t') \hat{\mathbf{d}}(t) - \hat{\mathbf{d}}(t) \rho(t) \hat{\mathbf{d}}(t')]. \end{aligned} \quad (\text{A11})$$

We make the two following additional approximations.

(1)  $\langle \hat{\mathbf{E}}_v^{(+)}(t) \hat{\mathbf{E}}_v^{(+)}(t') \rangle = \langle \hat{\mathbf{E}}_v^{(+)}(t') \hat{\mathbf{E}}_v^{(+)}(t) \rangle = \langle \hat{\mathbf{E}}_v^{(-)}(t) \hat{\mathbf{E}}_v^{(-)}(t') \rangle = \langle \hat{\mathbf{E}}_v^{(-)}(t') \hat{\mathbf{E}}_v^{(-)}(t) \rangle = 0$  (which is valid for an environment in thermodynamic equilibrium).

(2)  $\langle \hat{\mathbf{E}}_v^{(-)}(t) \hat{\mathbf{E}}_v^{(+)}(t') \rangle = \langle \hat{\mathbf{E}}_v^{(-)}(t') \hat{\mathbf{E}}_v^{(+)}(t) \rangle = 0$  (which is valid for optical frequencies).

Thus, only the first two terms remain in Eq. (A11), which reduces to

$$\frac{\partial \rho(t)}{\partial t} = -\frac{1}{\hbar^2} \int_0^t dt' \langle \hat{\mathbf{E}}_v^{(+)}(t) \hat{\mathbf{E}}_v^{(-)}(t') \rangle [\hat{\mathbf{d}}^\dagger(t) \hat{\mathbf{d}}(t') \rho(t) - \hat{\mathbf{d}}(t') \rho(t) \hat{\mathbf{d}}^\dagger(t)] + \langle \hat{\mathbf{E}}_v^{(+)}(t') \hat{\mathbf{E}}_v^{(-)}(t) \rangle [\rho(t) \hat{\mathbf{d}}^\dagger(t') \hat{\mathbf{d}}(t) - \hat{\mathbf{d}}(t) \rho(t) \hat{\mathbf{d}}^\dagger(t')]. \quad (\text{A12})$$

By using the property of the correlation function  $\langle \hat{\mathbf{E}}_v^{(+)}(t') \hat{\mathbf{E}}_v^{(-)}(t) \rangle = \langle \hat{\mathbf{E}}_v^{(+)}(t) \hat{\mathbf{E}}_v^{(-)}(t') \rangle^*$ , and noting the fact that  $[\rho(t) \hat{\mathbf{d}}^\dagger(t') \hat{\mathbf{d}}(t) - \hat{\mathbf{d}}(t) \rho(t) \hat{\mathbf{d}}^\dagger(t')] = [\hat{\mathbf{d}}^\dagger(t) \hat{\mathbf{d}}(t') \rho(t) - \hat{\mathbf{d}}(t') \rho(t) \hat{\mathbf{d}}^\dagger(t)]^\dagger$ , one can see that the second term in Eq. (A12) is actually the Hermitian conjugate (H.c.) of the first one. Therefore, we simply write Eq. (A12) as

$$\frac{\partial \rho(t)}{\partial t} = -\frac{1}{\hbar^2} \int_0^t dt' \langle \hat{\mathbf{E}}_v^{(+)}(t) \hat{\mathbf{E}}_v^{(-)}(t') \rangle [\hat{\mathbf{d}}^\dagger(t) \hat{\mathbf{d}}(t') \rho(t) - \hat{\mathbf{d}}(t') \rho(t) \hat{\mathbf{d}}^\dagger(t)] + \text{H.c.} \quad (\text{A13})$$

### 3. Master equation for an atomic $\Lambda$ transition

Equation (A13) is the starting point to calculate the dynamical evolution of any multilevel atom. Here, we proceed by writing explicitly the terms in the integrand using the expressions for  $\hat{\mathbf{d}}(t)$  and  $\hat{\mathbf{d}}^\dagger(t)$  from Eqs. (A2) and (A3), which corresponds to the  $\Lambda$  configuration with orthogonal transitions,

$$\hat{\mathbf{d}}^\dagger(t) \hat{\mathbf{d}}(t') \rho(t) = e^{i\omega_1(t-t')} \mathbf{d}_{01} |0\rangle \langle 0| \mathbf{d}_{01}^* \rho(t) + e^{i\omega_2(t-t')} \mathbf{d}_{02} |0\rangle \langle 0| \mathbf{d}_{02}^* \rho(t), \quad (\text{A14})$$

and by defining  $\rho_{00}(t) \equiv \langle 0| \rho(t) |0\rangle$  to simplify the expressions:

$$\begin{aligned} \hat{\mathbf{d}}(t') \rho(t) \hat{\mathbf{d}}^\dagger(t) = & + e^{i\omega_1(t-t')} \rho_{00}(t) \mathbf{d}_{01}^* |1\rangle \langle 1| \mathbf{d}_{01} + e^{i\omega_2(t-t')} \rho_{00}(t) \mathbf{d}_{02}^* |2\rangle \langle 2| \mathbf{d}_{02} + e^{i\omega_1 t} e^{-i\omega_2 t'} \rho_{00}(t) \mathbf{d}_{02}^* |2\rangle \langle 1| \mathbf{d}_{01} \\ & + e^{i\omega_2 t} e^{-i\omega_1 t'} \rho_{00}(t) \mathbf{d}_{01}^* |1\rangle \langle 2| \mathbf{d}_{02}. \end{aligned} \quad (\text{A15})$$

Substituting these expressions in Eq. (A13) and by factorizing the exponential terms, we get

$$\begin{aligned} \frac{\partial \rho(t)}{\partial t} = & -\frac{1}{\hbar^2} \int_0^t dt' \langle \hat{\mathbf{E}}_v^{(+)}(t) \hat{\mathbf{E}}_v^{(-)}(t') \rangle \times [e^{i\omega_1(t-t')} (\mathbf{d}_{01} |0\rangle \langle 0| \mathbf{d}_{01}^* \rho(t) - \rho_{00}(t) \mathbf{d}_{01}^* |1\rangle \langle 1| \mathbf{d}_{01}) \\ & + e^{i\omega_2(t-t')} (\mathbf{d}_{02} |0\rangle \langle 0| \mathbf{d}_{02}^* \rho(t) - \rho_{00}(t) \mathbf{d}_{02}^* |2\rangle \langle 2| \mathbf{d}_{02}) \\ & - e^{i\omega_1 t} e^{-i\omega_2 t'} \rho_{00}(t) \mathbf{d}_{02}^* |2\rangle \langle 1| \mathbf{d}_{01} - e^{i\omega_2 t} e^{-i\omega_1 t'} \rho_{00}(t) \mathbf{d}_{01}^* |1\rangle \langle 2| \mathbf{d}_{02}] + \text{H.c.} \end{aligned} \quad (\text{A16})$$

We now write:  $\langle \hat{\mathbf{E}}_v^{(+)}(t) \hat{\mathbf{E}}_v^{(-)}(t') \rangle = \langle \hat{\mathbf{E}}_v^{(+)}(t-t') \hat{\mathbf{E}}_v^{(-)}(0) \rangle$  (the correlation function only depends on the time difference). Making the change of variable  $\tau = t - t'$ , the next approximation is to make the upper limit tend to infinity. Equation (A16) becomes

$$\begin{aligned} \frac{\partial \rho(t)}{\partial t} = & -\frac{1}{\hbar^2} \int_0^\infty d\tau \langle \hat{\mathbf{E}}_v^{(+)}(\tau) \hat{\mathbf{E}}_v^{(-)}(0) \rangle \times [e^{i\omega_1 \tau} \langle \mathbf{d}_{01} | 0 \rangle \langle 0 | \mathbf{d}_{01}^* \rho(t) - \rho_{00}(t) \mathbf{d}_{01}^* | 1 \rangle \langle 1 | \mathbf{d}_{01} \rangle \\ & + e^{i\omega_2 \tau} \langle \mathbf{d}_{02} | 0 \rangle \langle 0 | \mathbf{d}_{02}^* \rho(t) - \rho_{00}(t) \mathbf{d}_{02}^* | 2 \rangle \langle 2 | \mathbf{d}_{02} \rangle \\ & - e^{i(\omega_1 - \omega_2)t} e^{i\omega_2 \tau} \rho_{00}(t) \mathbf{d}_{02}^* | 2 \rangle \langle 1 | \mathbf{d}_{01} - e^{i(\omega_2 - \omega_1)t} e^{i\omega_1 \tau} \rho_{00}(t) \mathbf{d}_{01}^* | 1 \rangle \langle 2 | \mathbf{d}_{02} \rangle] + \text{H.c.} \end{aligned} \quad (\text{A17})$$

We finally introduce the positive part of the correlation tensor as

$$\hat{\mathbf{C}}^{(+)}(\omega) \equiv \int_0^\infty d\tau \langle \hat{\mathbf{E}}_v^{(+)}(\tau) \hat{\mathbf{E}}_v^{(-)}(0) \rangle e^{i\omega \tau} \quad (\text{A18})$$

to get

$$\begin{aligned} \frac{\partial \rho(t)}{\partial t} = & -\Gamma_1 \langle 0 | \rho(t) - \rho_{00}(t) | 1 \rangle \langle 1 | \\ & -\Gamma_2 \langle 0 | \rho(t) - \rho_{00}(t) | 2 \rangle \langle 2 | \\ & + \Gamma_{21} e^{i(\omega_1 - \omega_2)t} \rho_{00}(t) | 2 \rangle \langle 1 | \\ & + \Gamma_{12} e^{i(\omega_2 - \omega_1)t} \rho_{00}(t) | 1 \rangle \langle 2 | + \text{H.c.} \end{aligned} \quad (\text{A19})$$

with the following definitions of the coefficients:

$$\Gamma_i \equiv \frac{1}{\hbar^2} \mathbf{d}_{0i}^* \cdot \hat{\mathbf{C}}^{(+)}(\omega_i) \cdot \mathbf{d}_{0i} \quad (\text{A20})$$

and

$$\Gamma_{ij} \equiv \frac{1}{\hbar^2} \mathbf{d}_{0i}^* \cdot \hat{\mathbf{C}}^{(+)}(\omega_i) \cdot \mathbf{d}_{0j}. \quad (\text{A21})$$

Remember that in the master equation above  $\rho(t)$  is still in the interaction picture, and we come back to the *Schrödinger picture* assuming furthermore that the transition energies are about the same,  $\omega_1 \simeq \omega_2 \equiv \omega_0$ :

$$\begin{aligned} \frac{\partial \rho(t)}{\partial t} = & -i\omega_0 | 0 \rangle \langle 0 | \rho(t) \\ & -\Gamma_1 \langle 0 | \rho(t) - \rho_{00}(t) | 1 \rangle \langle 1 | \\ & -\Gamma_2 \langle 0 | \rho(t) - \rho_{00}(t) | 2 \rangle \langle 2 | \\ & + \Gamma_{21} \rho_{00}(t) | 2 \rangle \langle 1 | + \Gamma_{12} \rho_{00}(t) | 1 \rangle \langle 2 | + \text{H.c.} \end{aligned} \quad (\text{A22})$$

In Eq. (A22), we have introduced the definitions of the coefficients

$$\Gamma_i \equiv \frac{1}{\hbar^2} \mathbf{d}_{0i}^* \cdot \hat{\mathbf{C}}^{(+)}(\mathbf{r}_0, \mathbf{r}_0, \omega_0) \cdot \mathbf{d}_{0i} \quad (\text{A23})$$

and

$$\Gamma_{ij} \equiv \frac{1}{\hbar^2} \mathbf{d}_{0i}^* \cdot \hat{\mathbf{C}}^{(+)}(\mathbf{r}_0, \mathbf{r}_0, \omega_0) \cdot \mathbf{d}_{0j} \quad (\text{A24})$$

defined in terms of the *positive part of the correlation tensor*  $\hat{\mathbf{C}}^{(+)}$  that reads

$$\hat{\mathbf{C}}^{(+)}(\mathbf{r}, \mathbf{r}', \omega) = \int_0^{+\infty} d\tau \langle \hat{\mathbf{E}}_v^{(+)}(\mathbf{r}, \tau) \hat{\mathbf{E}}_v^{(-)}(\mathbf{r}', 0) \rangle e^{i\omega \tau} \quad (\text{A25})$$

where the bracket indicates an ensemble average:

$$\langle \hat{\mathbf{E}}_v^{(+)}(\mathbf{r}, \tau) \hat{\mathbf{E}}_v^{(-)}(\mathbf{r}', 0) \rangle \equiv \text{Tr}_e[\rho_e(0) \hat{\mathbf{E}}_v^{(+)}(\mathbf{r}, \tau) \hat{\mathbf{E}}_v^{(-)}(\mathbf{r}', 0)]. \quad (\text{A26})$$

Using the mathematical relation

$$\mathcal{P}\left(\frac{1}{x}\right) = \frac{1}{x + i\epsilon} + i\pi \delta(x) \quad \text{with } \epsilon \rightarrow 0 \quad (\text{A27})$$

one can demonstrate that

$$\begin{aligned} \hat{\mathbf{C}}^{(+)}(\mathbf{r}, \mathbf{r}', \omega_0) \\ = \frac{1}{2} \hat{\mathbf{C}}(\mathbf{r}, \mathbf{r}', \omega_0) + \frac{i}{2\pi} \mathcal{P} \left\{ \int_0^{+\infty} d\omega \frac{\hat{\mathbf{C}}(\mathbf{r}, \mathbf{r}', \omega)}{\omega_0 - \omega} \right\} \end{aligned} \quad (\text{A28})$$

where  $\hat{\mathbf{C}}$  is the correlation tensor defined as

$$\hat{\mathbf{C}}(\mathbf{r}, \mathbf{r}', \omega) \equiv \int_{-\infty}^{+\infty} d\tau \langle \hat{\mathbf{E}}_v^{(+)}(\mathbf{r}, \tau) \hat{\mathbf{E}}_v^{(-)}(\mathbf{r}', 0) \rangle e^{i\omega \tau}. \quad (\text{A29})$$

Therefore, the coefficients  $\Gamma_i$  become

$$\Gamma_i = \frac{\gamma_i}{2} + i\Delta\omega_i \quad (\text{A30})$$

with

$$\gamma_i = \frac{1}{\hbar^2} \mathbf{d}_{0i}^* \cdot \hat{\mathbf{C}}(\mathbf{r}_0, \mathbf{r}_0, \omega_0) \cdot \mathbf{d}_{0i} \quad (\text{A31})$$

and

$$\Delta\omega_i = \frac{1}{2\pi\hbar^2} \mathcal{P} \left\{ \int_0^{+\infty} d\omega \frac{\mathbf{d}_{0i}^* \cdot \hat{\mathbf{C}}(\mathbf{r}_0, \mathbf{r}_0, \omega) \cdot \mathbf{d}_{0i}}{\omega_0 - \omega} \right\} \quad (\text{A32})$$

where  $\gamma_i$  can be interpreted as the decay rate on the transition  $|0\rangle \rightarrow |i\rangle$ , and  $\Delta\omega_i$  is the Lamb shift of the level  $|i\rangle$ .

In the following, we recast the Lamb shift into the transition frequency and reduce  $\hat{\mathbf{C}}^{(+)}(\mathbf{r}, \mathbf{r}', \omega_0)$  as

$$\hat{\mathbf{C}}^{(+)}(\mathbf{r}, \mathbf{r}', \omega_0) \equiv \frac{1}{2} \hat{\mathbf{C}}(\mathbf{r}, \mathbf{r}', \omega_0). \quad (\text{A33})$$

Therefore, the coefficients become

$$\Gamma_i = \frac{\gamma_i}{2} \quad \text{with} \quad \gamma_i = \frac{1}{\hbar^2} \mathbf{d}_{0i}^* \cdot \hat{\mathbf{C}}(\mathbf{r}_0, \mathbf{r}_0, \omega_0) \cdot \mathbf{d}_{0i} \quad (\text{A34})$$

and

$$\Gamma_{ij} = \frac{\kappa_{ij}}{2} \quad \text{with} \quad \kappa_{ij} = \frac{1}{\hbar^2} \mathbf{d}_{0i}^* \cdot \hat{\mathbf{C}}(\mathbf{r}_0, \mathbf{r}_0, \omega_0) \cdot \mathbf{d}_{0j}. \quad (\text{A35})$$

#### 4. Solution of the master equation

From the master equation, given in Eq. (A22), we obtain the following equations for the atomic populations  $\rho_{ii}(t)$  and

atomic coherences  $\rho_{ij}(t)$  with  $j \neq i$ :

$$\dot{\rho}_{ii}(t) = \gamma_i \rho_{00}(t) \quad \text{for } i = 1, 2, \quad (\text{A36})$$

$$\dot{\rho}_{00}(t) = -(\gamma_1 + \gamma_2) \rho_{00}(t), \quad (\text{A37})$$

$$\dot{\rho}_{i0}(t) = -\left(\frac{\gamma_1 + \gamma_2}{2} - i\omega_0\right) \rho_{i0}(t) \quad \text{for } i = 1, 2, \quad (\text{A38})$$

$$\dot{\rho}_{12}(t) = \kappa_{12} \rho_{00}(t), \quad (\text{A39})$$

where we used the fact that  $\kappa_{21}^* = \kappa_{12}$ . Note that these equations are also supplemented by their conjugates.

The atom is initially prepared in the excited state with the following initial conditions (at  $t = 0$ ):  $\rho_{00}(0) = 1$ ,  $\rho_{11}(0) = \rho_{22}(0) = 0$ , and  $\rho_{ij}(0) = 0$  for  $j \neq i$ . Solving Eqs. (A36) and (A37) with the initial conditions above is straightforward. With the initial condition  $\rho_{00}(0) = 1$ , Eq. (A37) gives

$$\rho_{00}(t) = e^{-(\gamma_1 + \gamma_2)t} \Rightarrow \rho_{00}(\infty) = 0. \quad (\text{A40})$$

Substituting it in Eqs. (A36) and carrying out the integration with the initial conditions  $\rho_{11}(0) = \rho_{22}(0) = 0$

gives

$$\rho_{11}(t) = \frac{\gamma_1}{\gamma_1 + \gamma_2} [1 - e^{-(\gamma_1 + \gamma_2)t}] \Rightarrow \rho_{11}(\infty) = \frac{\gamma_1}{\gamma_1 + \gamma_2}, \quad (\text{A41})$$

$$\rho_{22}(t) = \frac{\gamma_2}{\gamma_1 + \gamma_2} [1 - e^{-(\gamma_1 + \gamma_2)t}] \Rightarrow \rho_{22}(\infty) = \frac{\gamma_2}{\gamma_1 + \gamma_2}. \quad (\text{A42})$$

Furthermore, integration of Eq. (A38) together with the initial condition  $\rho_{ij}(0) = 0$  for  $j \neq i$  gives

$$\rho_{10}(t) = \rho_{20}(t) = 0 \quad \forall t. \quad (\text{A43})$$

Finally, for the coherence  $\rho_{12}(t)$  given by Eq. (A39), substituting the expression of  $\rho_{00}(t)$  [Eq. (A40)] in Eq. (A39) gives

$$\dot{\rho}_{12}(t) = \kappa_{12} e^{-(\gamma_1 + \gamma_2)t} \quad (\text{A44})$$

and after integration, together with the initial condition  $\rho_{12}(0) = 0$ , we find

$$\rho_{12}(t) = \frac{\kappa_{12}}{\gamma_1 + \gamma_2} [1 - e^{-(\gamma_1 + \gamma_2)t}], \quad (\text{A45})$$

and for  $t \rightarrow \infty$

$$\rho_{12}(\infty) = \frac{\kappa_{12}}{\gamma_1 + \gamma_2}. \quad (\text{A46})$$

- 
- [1] J.-M. Raimond and S. Haroche, *Exploring the Quantum* (Oxford University, New York, 2006).
- [2] D. G. Baranov, M. Wersall, J. Cuadra, T. J. Antosiewicz, and T. Shegai, *ACS Photonics* **5**, 24 (2017).
- [3] G. Hétet, L. Slodička, A. Glätzle, M. Hennrich, and R. Blatt, *Phys. Rev. A* **82**, 063812 (2010).
- [4] U. Dörner and P. Zoller, *Phys. Rev. A* **66**, 023816 (2002).
- [5] J. Kästel and M. Fleischhauer, *Phys. Rev. A* **71**, 011804(R) (2005).
- [6] J. Eschner, C. Raab, F. Schmidt-Kaler, and R. Blatt, *Nature (London)* **413**, 495 (2001).
- [7] P. K. Jha, X. Ni, C. Wu, Y. Wang, and X. Zhang, *Phys. Rev. Lett.* **115**, 025501 (2015).
- [8] P. K. Jha, N. Shitrit, X. Ren, Y. Wang, and X. Zhang, *Phys. Rev. Lett.* **121**, 116102 (2018).
- [9] P. Lalanne and P. Chavel, *Laser Photonics Rev.* **11**, 1600295 (2017).
- [10] P. Genevet, F. Capasso, F. Aieta, M. Khorasaninejad, and R. Devlin, *Optica* **4**, 139 (2017).
- [11] G. S. Agarwal, *Phys. Rev. Lett.* **84**, 5500 (2000).
- [12] G. S. Agarwal and A. K. Patnaik, *Phys. Rev. A* **63**, 043805 (2001).
- [13] G.-X. Li, F.-L. Li, and S.-Y. Zhu, *Phys. Rev. A* **64**, 013819 (2001).
- [14] Y. Yang, J. Xu, H. Chen, and S. Zhu, *Phys. Rev. Lett.* **100**, 043601 (2008).
- [15] L. Sun and C. Jiang, *Opt. Express* **24**, 7719 (2016).
- [16] S. Hughes and G. S. Agarwal, *Phys. Rev. Lett.* **118**, 063601 (2017).
- [17] D. Suter, *The Physics of Laser-Atom Interactions*, Cambridge Studies in Modern Optics, Vol. 19 (Cambridge University, Cambridge, England, 1997).
- [18] E. Togan, Y. Chu, A. Trifonov, L. Jiang, J. Maze, L. Childress, M. G. Dutt, A. S. Sørensen, P. Hemmer, A. S. Zibrov *et al.*, *Nature (London)* **466**, 730 (2010).
- [19] S. M. Barnett and P. M. Radmore, *Methods in Theoretical Quantum Optics*, Oxford Series in Optical and Imaging Sciences, Vol. 15 (Oxford University, New York, 2002).
- [20] H. J. Carmichael, *Statistical Methods in Quantum Optics 1: Master Equations and Fokker-Planck Equations* (Springer, New York, 2013).
- [21] G. Balasubramanian, P. Neumann, D. Twitchen, M. Markham, R. Kolesov, N. Mizuochi, J. Isoya, J. Achard, J. Beck, J. Tissler, V. Jacques, P. R. Hemmer, F. Jelezko, and J. Wrachtrup, *Nat. Mater.* **8**, 383 (2009).
- [22] M. O. Scully and M. S. Zubairy, *Quantum Optics* (Cambridge University, Cambridge, England, 1997).
- [23] G. Jaeger, A. Shimony, and L. Vaidman, *Phys. Rev. A* **51**, 54 (1995).
- [24] B.-G. Englert, *Phys. Rev. Lett.* **77**, 2154 (1996).
- [25] V. Yannopoulos, E. Paspalakis, and N. V. Vitanov, *Phys. Rev. Lett.* **103**, 063602 (2009).
- [26] W. Jhe, A. Anderson, E. A. Hinds, D. Meschede, L. Moi, and S. Haroche, *Phys. Rev. Lett.* **58**, 666 (1987).
- [27] T. Taillandier-Loize, J. Baudon, G. Dutier, F. Perales, M. Boustimi, and M. Ducloy, *Phys. Rev. A* **89**, 052514 (2014).
- [28] M. Boustimi, B. Viaris de Lesegno, J. Baudon, J. Robert, and M. Ducloy, *Phys. Rev. Lett.* **86**, 2766 (2001).
- [29] I. Thanopoulos, V. Karanikolas, and E. Paspalakis, *Opt. Lett.* **44**, 3510 (2019).
- [30] S. Evangelou, V. Yannopoulos, and E. Paspalakis, *Phys. Rev. A* **83**, 055805 (2011).
- [31] I. Thanopoulos, V. Yannopoulos, and E. Paspalakis, *Phys. Rev. B* **95**, 075412 (2017).

- [32] V. Karanikolas and E. Paspalakis, *J. Phys. Chem. C* **122**, 14788 (2018).
- [33] S. Sun, K.-Y. Yang, C.-M. Wang, T.-K. Juan, W. T. Chen, C. Y. Liao, Q. He, S. Xiao, W.-T. Kung, G.-Y. Guo *et al.*, *Nano Lett.* **12**, 6223 (2012).
- [34] A. Pors, O. Albrektsen, I. P. Radko, and S. I. Bozhevolnyi, *Sci. Rep.* **3**, 2155 (2013).
- [35] G. Zheng, H. Mühlenbernd, M. Kenney, G. Li, T. Zentgraf, and S. Zhang, *Nat. Nanotechnol.* **10**, 308 (2015).
- [36] P. K. Jha, N. Shitrit, J. Kim, X. Ren, Y. Wang, and X. Zhang, *ACS Photonics* **5**, 971 (2017).
- [37] J. Hugonin and P. Lalanne, RETICOLO software for grating analysis, Institute d'Optique, Palaiseau, France, 2005.
- [38] M. Moharam, E. B. Grann, D. A. Pommet, and T. Gaylord, *J. Opt. Soc. Am. A* **12**, 1068 (1995).
- [39] L. Li, *J. Opt. Soc. Am. A* **14**, 2758 (1997).
- [40] P. Lalanne and M. P. Jurek, *J. Mod. Opt.* **45**, 1357 (1998).
- [41] E. Popov and M. Nevière, *J. Opt. Soc. Am. A* **17**, 1773 (2000).
- [42] W. Luo, S. Xiao, Q. He, S. Sun, and L. Zhou, *Adv. Opt. Mater.* **3**, 1102 (2015).
- [43] S. Larouche and D. R. Smith, *Opt. Lett.* **37**, 2391 (2012).
- [44] S. Pancharatnam, in *Proceedings of the Indian Academy of Sciences: Section A* (Springer, New York, 1956), Vol. 44, pp. 398–417.
- [45] M. V. Berry, *J. Mod. Opt.* **34**, 1401 (1987).
- [46] E. Lassalle, N. Bonod, T. Durt, and B. Stout, *Opt. Lett.* **43**, 1950 (2018).
- [47] J. R. Ong, H. S. Chu, V. H. Chen, A. Y. Zhu, and P. Genevet, *Opt. Lett.* **42**, 2639 (2017).
- [48] S. Jafar-Zanjani, S. Inampudi, and H. Mosallaei, *Sci. Rep.* **8**, 11040 (2018).
- [49] N. Schmitt, N. Georg, G. Brière, D. Loukrezis, S. Héron, S. Lanteri, C. Klitis, M. Sorel, U. Römer, H. De Gersem *et al.*, *Opt. Mater. Express* **9**, 892 (2019).
- [50] J. Yang and J. A. Fan, *Opt. Lett.* **42**, 3161 (2017).
- [51] A. Y. Piggott, J. Lu, T. M. Babinec, K. G. Lagoudakis, J. Petykiewicz, and J. Vučković, *Sci. Rep.* **4**, 7210 (2014).
- [52] F. Callewaert, V. Velez, P. Kumar, A. Sahakian, and K. Aydin, *Sci. Rep.* **8**, 1358 (2018).